Nanoscale Advances

Accepted Manuscript

This article can be cited before page numbers have been issued, to do this please use: J. Huang, J. Chen, Z. Yin and J. Wu, *Nanoscale Adv.*, 2020, DOI: 10.1039/D0NA00211A.

ROYAL SOCIETY OF CHEMISTRY

rsc.li/nanoscale-advances

View Article Online
DOI: 10.1039/D0NA00211A

Nanoscale Advances

ARTICLE

A hierarchical porous P-doped carbon electrode through hydrothermal carbonization of pomelo valves for high-performance supercapacitors

Received 00th January 20xx,
Accepted 00th January 20xx

DOI: 10.1039/x0xx00000x

Jing Huang, [§] *[a] Jie Chen, [§ a] Zhenyao Yin[a] and Jinggao Wu[b]

Porous carbon materials are synthesized from pomelo valves by the hydrothermal activation of H_3PO_4 followed by the simple carbonization. The as-synthesized hierarchically porous carbon electrode indicates a high specific capacitance of 966.4 F g^{-1} at 1 A g^{-1} and an ultra-high stability of 95.6% even after 10 000 cycles. Moreover, the supercapacitor also demonstrates a maximum energy of 36.39 W h kg^{-1} and a maximum power of 33.33 kW kg^{-1} with an energy retention of 25.56 W h kg^{-1}, which paves the way for the development of high-performance, green supercapacitors for advanced energy storage systems.

1. Introduction

The rapidly expanding market for portable electronic devices and hybrid vehicles is stimulating intensive research for developing cost-effective and eco-friendly energy storage devices[1-3]. Energy storage devices play a crucial role in enabling the transition from fossil fuels to renewable energy sources[4-6]. Supercapacitors feature ultrafast charge/discharge rates, high power densities, low maintenance costs, and long cycling lives as the promising energy storage devices for electric vehicles, portable electronics, and stationary energy storage devices. They are classified into electrical double layer capacitors (EDLCs) and pseudocapacitors according to the different capacitive mechanisms[7-10].

Owing to the capacitance is proportional to the surface area of the electrode, carbons materials usually have good conductivities, abundant morphologies, and tunable surface properties by doping and/or surface functionalization, which are the main option to explore the advanced EDLC electrode materials[11-13]. Various carbon materials such as activated carbon (AC), carbon nanotubes (CNTs), and graphene have been intensively studied, which demonstrate that there is still plenty room to further improve the supercapacitive performance with the new carbon architecture[14-16]. Especially, porous carbon materials derived from biomasses have attracted increasing attention due to their availability and chemical composition, such as environmentally friendly disposal and cost decrease associated with activated carbon production[17-20]. More importantly, most biomasses contain abundant hetero-atoms (e.g., oxygen, nitrogen, and sulfur) that can be in situ doped into carbon matrices during carbonization processes. These heteroatoms not only increase the wettability of the carbon material, but also contribute pseudo-capacitance[21-24].

Several studies have dealt with functionalization of activated carbon to achieve the desired properties by grafting different surface groups at appropriate oxidation states[25-27]. Among the modification of this AC property, doping the carbon matrix with heteroatoms, such as oxygen, nitrogen, boron, sulfur, and phosphorus, is the most effective way to tailor the electronic structures and improve the surface properties. Oxygen functionalities are often present on the carbon surface, and their effect on the capacitive performance must be considered as they take part in the Faradic interactions and thus significantly increase the specific capacitance of carbons in acidic aqueous supercapacitors. The conjugation of the lone-pair electrons of N and the graphitic π-bonds of carbon materials can further distort the carbon structure to create defects and available active sites, which has been extensively and deeply studied. However, the functional mechanism of the phosphorus configuration in the skeleton of P-doped carbon materials remains unclear[28-36].

In this context, we report a novel type of porous P-enriched carbon material derived from pomelo valves through hydrothermal carbonization of H_3PO_4 (Scheme 1). By the way, the chemical bonding states of phosphorus with carbon and oxygen has been systematically explored and the type of P-doped configuration with the electrochemical performance has also been correlated. We expect that this research will pave the way for the identification of P-doped configuration and provide the feasibility of the rational design of P-doped carbon materials with superior performance in many fields.

[a] State Key Laboratory of Silkworm Genome Biology, Key Laboratory of Sericultural Biology and Genetic Breeding, Ministry of Agriculture and Rural Affairs, College of Biotechnology, Southwest University, Chongqing 400715, P. R. China
[b] Key Laboratory of Rare Earth Optoelectronic Materials&Devices, College of Chemistry and Materials Engineering, Huaihua University, Huaihua 418000, PR China
[§] Equal contribution to this work
† Footnotes relating to the title and/or authors should appear here.
Electronic Supplementary Information (ESI) available: [details of any supplementary information available should be included here]. See DOI: 10.1039/x0xx00000x

View Article Online
DOI: 10.1039/D0NA00211A

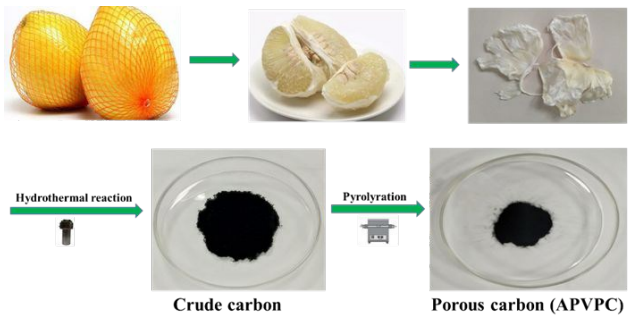

Scheme 1Synthesis of porous carbon from waste pomelo valves

2. Experimental section

2.1 Materials and Methods

2.1.1 Materials and reagent

Pomelo was purchased from a local supermarket in China and the pomelo valves were collected by means of shucking off the pomelo peel and removing the edible portions as well as the pomelo seeds. Nafion solution, acetylene black, poly (tetrafluoroethylene) (PTFE), ethanol were purchased from Sigma-Aldrich. Potassium hydroxide (KOH) and all others reagents were obtained from Adamas-beta®. All chemicals were used without further purification.

2.1.2 Synthesis of the activated pomelo valves-derived porous carbon (APVPC)

The waste pomelo valves were air-dried and cut into pieces, prior to the hydrothermal carbonization process. Within the underlying hydrothermal treatment, 1 g of pomelo valves were put into a Teflon-lined stainless steel autoclave wherein a 70 mL of homogeneous H_3PO_4 (1M, 5M, 10M, 16M) solution was contained. Subsequently, the autoclave was sealed and placed still in an electric oven at a temperature of 120 ℃ for (1, 3, 6) h. After cooling down to room temperature naturally, the samples were centrifuged and freeze-dried. Next, the products were calcined at 700 ℃ under Ar flow for 3 h. Finally, the black carbon material was washed with hot water several times and dried in an oven at 80 °C for 12 hours to afford APVPC. The samples were denoted as APVPC-1 (1h, 16M H_3PO_4), APVPC-2 (3h, 16M), APVPC-3(6h, 16M), APVPC-4(3h, 1M), APVPC-5 (3h, 5M) and APVPC-6 (3h, 10M). For comparison, the air-dried pomelo valves with deionized water treatment were carried out according to the similar procedure and the obtained porous carbon was denoted as PVPC.

2.2 Characterizations

The XRD patterns of all samples were recorded using powder X-ray diffraction (Shimadzu XRD-7000). The morphologies of the porous carbon materials were characterized using field emission scanning electron microscopy (FESEM, JSM-7800F) and high-resolution transmission electron microscopy (TEM, JEOL 2100) equipped with energy dispersive spectroscopy (EDS). Elemental analysis was carried out in a LECO CHNS microanalyzer. Nitrogen sorption isotherms were obtained using an Autosorb-1 (Quantachrome Instruments). The specific surface area was calculated by the modified Brunauer-Emmet-Teller (BET) method. The pore size distributions and the pore volume were analyzed from the adsorption branch isotherms by density functional theory (DFT) method. Moreover, the total pore volume (Vt) was estimated from the amount adsorbed at a relative pressure P/P_0 of 0.990. The micropore volume (Vmic) and micropore surface area (Smic) were determined by the t-plot theory. Raman spectra were acquired with a Jobin-Yvon HR 800 spectrometer. X-ray photoelectron spectroscopy (XPS) measurements were performed on a Thermo Fisher Scientific (Escalab 250xi, USA). Fourier transform infrared (FT-IR) spectra were recorded on a Thermo Scientific Nicolet iS 50 spectrometer.

2.3 Electrochemical measurements

For the three-electrode system, the working electrode was fabricated through the dispersion of active carbon in the mixed solution of nafion and ethanol (1:20) dropping on the glassy carbon electrode; platinum foil and Hg/HgO were applied as the counter and reference electrodes, respectively. The electrochemical capacitive performance was performed on an electrochemical workstation (Shanghai Chenhua Instrument Co. Ltd, China, CHI660D) at room temperature.

For the three-electrode system, the gravimetric specific capacitance, C_{sp} (F g^{-1}), can be calculated according to the following equations:

$$C_{sp} = I \times \triangle t/m \times \triangle V \quad (1)$$

where I is the discharge current (A), Δt is the discharge time (s), ΔV is the voltage (V), and m is the mass of the active materials (g).

For the two-electrode system, the working electrodes were prepared by mixing electroactive material, acetylene black, and polytetrafluoroethylene (PTFE) binder with a weight ratio of 8 : 1 : 1, followed by coating on foamed Ni grids ((1 cm × 1 cm) and pressing under a pressure of 20 MPa as well as drying overlight at 80 °C. The mass of the active material loading in each working electrode was measured to be 2~3 mg cm^{-2}. The symmetrical capacitor was assembled using two nearly identical working electrodes and a glass fiber membrane (Waterman, GF/B) as a separator as well as 3 M KOH aqueous solution as the electrolyte.

For the two-electrode system, the gravimetric specific capacitance, C_{sp}(F g^{-1}), for a single electrode was calculated from each galvanostatic charge-discharge (GCD) curve as the following equation:

$$C_{sp} = 2I \times \triangle t/m \times \triangle V \quad (2)$$

where C_{sp} (F g^{-1}) is specific capacitance based on the mass of the active carbons, where I (A) is the discharge current, Δt (s) is the discharge time, ΔV (V) is the voltage change excluding the IR drop during the discharge process, and m (g) is the loading of the active material in each working electrode.

The energy density E (W h kg^{-1}) and the power density P (W kg^{-1}) were estimated by using the following equations:

$$E = C_{sp}V^2/(2\times3.6) \quad (3)$$

$$P = 3600E/\Delta t \quad (4)$$

where C_{sp} (F g^{-1}) is the specific capacitance of a single electrode, V (V) is the voltage change during the discharge process, and Δt (s) is the discharge time.

View Article Online
DOI: 10.1039/D0NA00211A

3. Results and Discussions

3.1 Material Characterization

The detailed synthesis procedure of the APVPC is described in Scheme 1. It is noted that H_3PO_4 activation plays an important role in the development of the pore structure in APVPC. In particular, the specific surface area (SSA) and the pore structure of the product are obviously influenced by the concentration of H_3PO_4. The sample produced with 85% H_3PO_4 is selected as a typical sample for characterization and used for SCs unless otherwise specified.

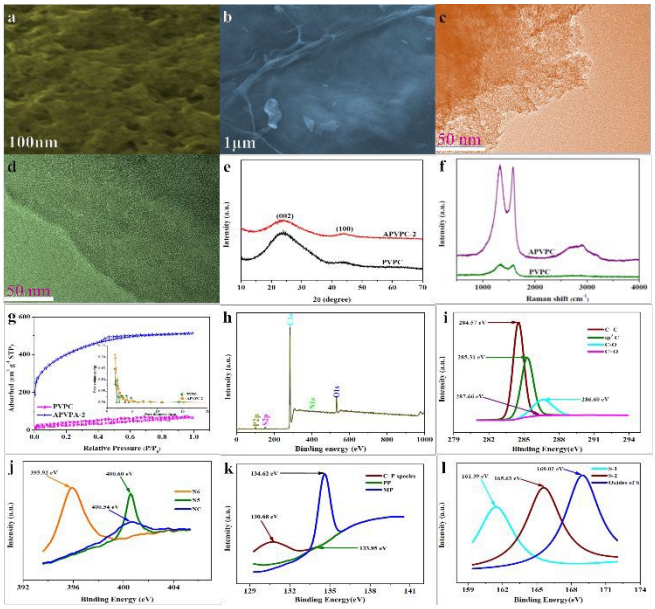

Fig.1 (a) SEM images of APVPC-2. (b) SEM images of PVPC. (c) TEM images of APVPC-2. (d) TEM images of PVPC. (e) XRD patterns of PVPC and APVPC-2. (f) Raman spectrum of PVPC and APVPC-2. (g)N_2 adsorption/desorption isotherms and the pore size distribution of APVPC-2 and PVPC. (h) XPS survey spectrum of APVPC-2. (i) High resolution C 1s of APVPC-2. (j) High resolution N 1s of APVPC-2. (k) High resolution P 2p of APVPC-2. (l) High resolution S 2p of APVPC-2.

Scanning electron microscopy (SEM) images (**Fig. 1a**) reveal that the APVPC-2 is made up of many carbon flakes with numerous uniformly sized mesopores and micropores through carbonizing the gelatinous tissue of pomelo valves, which are favorable for ion transport. On account of SEM images of APVPC-2, the PVPC (**Fig. 1b**) exhibits monolithic morphology, implying that the activation of H_3PO_4 could help to form thin sheets of carbon and to create a porous structure. High resolution TEM images of the APVPC-2 (**Fig. 1c**) demonstrates that the APVPC-2 consists of many carbon flakes with numerous nanopores of 1-3 nm in size, which contributes to a super high surface area. In addition to the connected thin layers, there are many amorphous carbon particles about 20 nm in diameter interconnected tightly, which are conductive to a high-rate-performance supercapacitor for facilitating the diffusion of electrolyte ions[37]. Compared with APVPC-2, TEM images of PVPC (**Fig. 1d**) indicate the primarily defective micro- and mesoporous morphology surrounded by curved carbon, which confirms a highly disordered structure[38].

The X-ray diffraction (XRD) (**Fig. 1e**) patterns of the samples demonstrate two characteristic peaks located at 2θ of 23.12° and 43.8°, corresponding to the (002) and (100) planes of graphitic carbon and the barely discernable peaks, respectively. The broad diffraction peak of carbon demonstrates that the highly amorphous and disordered nature of porous carbon. Further, the high intensity in the low angle region may be ascribed to the existence of abundant micropores[39]. Compared with the spectra of APVPC-2, we can see that the water residual in biomass tissue might be effective for increasing porosity as the spectra of PVPC show a broader peak[40]. On account of the Raman spectra for APVPC-2 (**Fig. 1f**), two peaks located at about 1331 and 1584 cm^{-1} correspond to D (disordered carbon) and G (graphitic carbon) bands, respectively. The intensity ratio between D and G bands (I_D/I_G) is summarized in **Fig. S2**. The I_D/I_G ratio obviously decreases from 1.051 for PVPC to 1.022 for APVPC-2 (**Fig. S2a**), confirming that deeper activation has lessened the presence of defects and disordered section in APVPC-2 sample[41], which agree well with the XRD analysis and TEM images. However, the G band of APVPC-2 shows a more redshift to 1584 cm^{-1} compared to pristine PVPC (1594 cm^{-1}), which could be attributed to n-type substitutional doping of porous carbon and further confirm the heteroatom doping into the carbon framework[23]. As for the effect of reaction time, the I_D/I_G ratio of APVPC-2 (1.022, 3h) is obviously higher than that of APVPC-1 (0.948, 1h) and APVPC-3 (0.96, 6h) (**Fig. S2b-c**), which indicates that the defection intensity gradually develop into stronger, and then turns slightly weaker at longer activation time. In addition, the I_D/I_G ratio increases along with the concentration of H_3PO_4 (1M vs 5M vs 10M vs 16 M H_3PO_4; APVPC-4 vs APVPC-5 vs APVPC-6 vs APVPC-2; 0.927 vs 0.941 vs 0.958 vs 1.022) (**Fig. S2d-e**), which demonstrates that the graphitization intensity gradually becomes weaker. Based on the aforementioned results, the higher values for APVPC-2 indicate the highly disordered nature and hetero atom doping and further could contribute to the increases in electrical conductivity after hetero atom dopant, which is due to broadening of van-Hove singularities in the density of states making the Fermi level to shift towards conduction bands[8].

Based on the apparent hysteresis loop at relative pressure P/P_0 from 0.4 to 0.9(**Fig. 1g**), APVPC-2 possesses a well-ordered mesoporous structure, which agree well with the pore size distribution calculated by the Barrett-Joyner-Halenda (BJH) model. Compared with PVPC, APVPC-2 has the widest pore size distribution, which results in a high nitrogen BET specific surface area of 1432.125 $m^2\ g^{-1}$ (vs 96.939 $m^2\ g^{-1}$) with a pore volume of 0.718 $cm^3\ g^{-1}$ (0.104 $cm^3\ g^{-1}$). The SSA contributed by mesopores is determined to be about 115 $m^2\ g^{-1}$. It is worth noting that the surface area of APVPC-2 is much higher than that of PVPC, further confirming that the activation of H_3PO_4 could effectively make holes and further increase specific surface area. As shown in **Table 1**, all samples have both micropores (0-2 nm) and mesopores (2-50 nm), and the pore size mainly focuses on ~0.718 nm. Increasing the activation time from 1h to 3h generates a huge amount of gas (CO and CO_2) from activation agent (H_3PO_4) that favorably increases the textural properties (1h vs 3h; 245.82 $m^2\ g^{-1}$, 0.135 $cm^3\ g^{-1}$ vs 1432.125 $m^2\ g^{-1}$, 0.718 $cm^3\ g^{-1}$; APVPC-1 vs APVPC-2). However, further increasing the activation time to 6h makes the pores to

View Article Online
DOI: 10.1039/D0NA00211A

collapse, unfavorably resulting in the decrease of the textural properties (3h vs 6h; 1432.125 $m^2 g^{-1}$, 0.718 $cm^3 g^{-1}$ vs 678.56 $m^2 g^{-1}$, 0.374 $cm^3 g^{-1}$; APVPC-2 vs APVPC-3). Additionally, the textural properties also increase along with the concentration of H_3PO_4 (1M vs 5M vs 10M vs 16M; from 373.664 to 1432.125 $m^2 g^{-1}$, from 0.144 $cm^3 g^{-1}$ to 0.718 $cm^3 g^{-1}$; APVPC-4 vs APVPC-5 vs APVPC-6 vs APVPC-2). It is widely accepted that mesopores and macropores can provide electrolyte ion transport and diffusion channels, and the micropores offer space for ion storage energy[42]. High porosity greatly maximizes the ion adsorption sites, which could lead to high capacitance and providing quick electrolyte diffusion into deeper pores[43]. Therefore, the as-prepared APVPC-2 should have a high specific capacitance and rate capability when applied as the electrode material in supercapacitors.

Table 1 Summary of BET characteristics of activated carbons

Sample	S_{BET}[a] ($m^2 g^{-1}$)	V_{tot}[b] ($cm^3 g^{-1}$)	S_{mi}[c] ($m^2 g^{-1}$)	S_{me}[d] ($m^2 g^{-1}$)	S_{ma}[e] ($m^2 g^{-1}$)	V_{mi}[f] ($cm^3 g^{-1}$)	V_{me}[g] ($cm^3 g^{-1}$)	V_{ma}[h] ($cm^3 g^{-1}$)
PVPC	96.939	0.104	12.67	63.28	20.989	0.0162	0.0623	0.0255
APVPC-1	245.82	0.135	86.132	105.62	54.068	0.0138	0.0461	0.0751
APVPC-2	1432.125	0.718	349.06	969.377	113.688	0.175	0.486	0.058
APVPC-3	678.56	0.374	213.62	268.53	196.41	0.102	0.153	0.119
APVPC-4	373.664	0.144	121.56	134.89	117.214	0.319	0.157	0.255
APVPC-5	421.694	0.224	163.72	136.26	121.714	0.0631	0.116	0.0449
APVPC-6	631.502	0.624	168.42	251.68	211.402	0.168	0.235	0.221

[a] S_{BET}: BET surface area; [b] V_{tot}: total volume; [c] S_{mi}: micropore surface area; [d] S_{me}: mesopore surface area; [e] S_{ma}: macropore surface area; [f] V_{mi}: micropore volume; [g] V_{me}: mesopore volume; [h] V_{ma}: macropore volume.

For more information on elemental chemical states of the heteroatoms in the APVPC-2, X-ray photoelectron spectroscopy (XPS) (**Fig. 1h**) is carried out and indicates five peaks at about 283.99, 399.94, 531.49, 128.12 and 163.8 eV corresponding to the C 1s, N 1s, O 1s, P 2p and S2p peaks, respectively. The relative percentages of the carbon species are given in **Table 2**. Results of elemental analysis reveal that the APVPC-2 mainly consists of C, N, O, P and S elements, and their contents are 62.86, 3.94, 32.28, 0.74 and 0.17 atom %, respectively. While for PVPC, XPS spectrum also shows five peaks for C 1s, N 1s, O 1s, P 2p and S2p peaks at about 283.99, 399.94, 531.49, 128.12 and 163.8 eV respectively. Meanwhile, the elemental contents for C, N, O, P and S are 91.72, 0.52, 7.63, 0.06 and 0.08%, respectively. Other possible metal impurities from biomass source are below the detection limit; these could have been removed during the post-acid washing process. The high resolution C 1s spectra for APVPC-2 (**Fig. 1i**) have been resolved into four peaks centering at around 284.57, 285.31, 286.60, and 287.66 eV, which belong to C=C, sp^3C, C-O and C=O[44], respectively. Moreover, the deconvoluted N 1s spectra (**Fig. 1j**) contain three peaks, pyridinic-N (N-6, 395.92 eV), pyrrolic-N (N-5, 400.60 eV) and amides/amines or nitrile N (NC, 400.54 eV)[45], which indicates the presence of nitrogen and further could improve the wettability and provide a large number of active sites for adsorption. On account of the $2p_{3/2}$ spectra (**Fig. 1k**), the three peaks at 130.68 eV, 133.93 eV and 134.62 eV can be assigned to C-P species, pyrophosphate/ polyphosphate (PP) and monophosphate/metaphosphate (MP) groups[46], respectively. After hydrothermal carbonization of pomelo valves through H_3PO_4-activation, the content of P is increased from 0.06 (PVPC) to 0.74 (APVPC-2), which confirms the phosphorus-doping of porous carbon successfully. In addition, the high-resolution S 2p spectrum (**Fig. 1l**) indicates three peaks at 161.39 and 165.63 as well as 169.02 eV, which are attributed to C=S and C-S bonds as well as the oxides of sulfur[47]. Thus, the XPS results also demonstrate the existence of hetero atoms such as N, O, P and S-containing functional groups in the samples. These functional groups may participate in the Faradaic reactions that increase the pseudo-capacitance and improve the wettability of the APVPC-based electrodes in the aqueous electrolytes[48].

Table 2 XPS analysis of the PVPC and APVPC-2

Samples	C (%)	N (%)	O (%)	P (%)	S (%)
PVPC	91.72	0.52	7.63	0.06	0.08
APVPC-2	62.86	3.94	32.28	0.74	0.17

Fourier transform infrared (FT-IR) spectroscopy is used to identify the surface functional groups of the as-synthesized samples (**Fig. S1f**). The absorptions at 3443, 2978, 1654, 1048, 1078 and 671cm^{-1} are attributed to the -NH, -C-H, -C=O, C-OH, C=S, and C-P[49], respectively. From the above FT-IR analysis, it could be deduced that oxygen-, nitrogen-, phosphorus- and sulphur-containing groups may exist in the samples, which agrees well with XPS results. On account of the aforementioned characterization, the carbon materials APVPC-2 derived from pomelo valves are provided with more preferential electrode material for supercapacitors by virtue of high surface area and 3D interconnected porous structure as well as heteroatom doping.

On account of the aforementioned investigation, we propose a formation mechanism of porous carbon nanosheets. The pomelo valves possess a net like structure consisting of a large number of polymeric cellulose. Owing to substantial hydrophilic functional groups such as hydroxy and carbonyl groups, the molecules of the polymeric cellulose in the pomelo valves could adsorb amounts of water molecules. In the activation process, H_3PO_4 vibrate violently in water to refrain the adjacent cell walls from agglomeration, and then the atoms decomposed from the molecules of polysaccharide connect together in situ to form

ultrathin nanosheets and rich pores. During the subsequent high-temperature carbonizing process, the polymeric cellulose is hydrolyzed to oligosaccharide along with gas evolution, which could contribute to forming a porous structure.

3.2 Electrochemical Behaviors

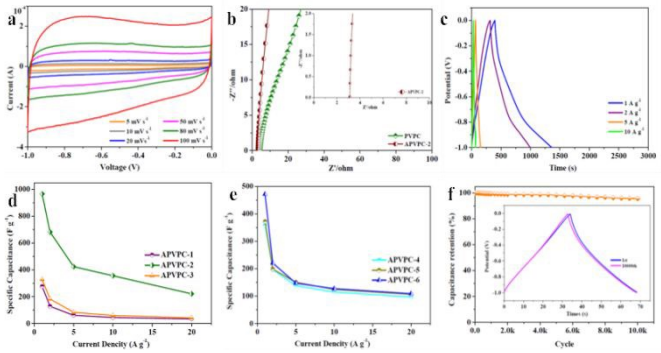

Fig. 2 (a) CV curves of APVPC-2 at different scan rates. (b) Nyquist plots of PVPC and APVPC-2. (c) Galvanostatic charge/discharge curves of APVPC-2 at different current densities. (d) Capacitances of APVPC samples prepared under different reaction times at different current densities. (e) Capacitances of APVPC samples prepared under different concentration of H_3PO_4 at different current densities. (f) Cycling performance of APVPC-2 at 10 A g^{-1}. The inset shows the GCD curves of the 1st and 10,000th cycle.

Ascribed in **Fig. 2a**, cyclic voltammetry (CV) curves of the APVPC-2 electrode demonstrates perfect rectangular shapes with obvious hump at low potential region, which confirms an indicative of the combination effects of electric double-layer capacitance (EDLC) and pseudo-capacitance due to the existence of active heteroatoms[45]. Even with an increase in scan rates from 5 to 100 mV s^{-1}, the APVPC-2 electrode still maintains perfect rectangular-shaped profiles, indicating faster kinetics in the porous carbon by virtue of the openness in structure resulting in fast ion transportation inside the pores[50]. On account of CV curves at 100 mV s^{-1} correlated with the capacitance of an electrode, APVPC-2 demonstrates the larger rectangular shape of the CV curves than other materials (**Fig. S3a-b**), suggesting the highest capacitance, which is consistent with the capacitance calculated by GCD curves. This could be attributed to its broader PSD and higher mesoporosity of APVPC-2 that is conducive to facile, fast electrolyte ion transport and shorten the diffusion distances from electrolyte to the inner micropore surface[51].

Electrochemical impedance spectroscopy (EIS) is also a critical technique to further study the electrochemical performance of the samples. According to the Nyquist plots of APVPC-2 (**Fig. 2b**) in 3 M KOH, the steep linear curve of APVPC-2 in the low-frequency region is closer to a vertical line than that of PVPC, which reveals that the H_3PO_4-activation can improve the capacitive behavior effectively. In contrast to PVPC, APVPC-2 indicates a larger slope of the straight line in Nyquist plots, which reveals lower diffusive resistance (W). At low frequency, electrolyte ions could penetrate inside the porous ACs and access to more electrode surface thereby contributing to high capacitance value. However, at high frequency, electrolyte ions can only access to the surface of carbon materials whereas the inner pores are not accessible that resulting in sharp decrease in the capacitance[52]. Meanwhile, the internal cell resistance (real Z' axis from Nyquist plots) is 3.12 Ω (56.25 kHz) for APVPC-2 and 4.408 Ω (68.12 kHz) for PVPC. Moreover, pseudocapacitance originating from Faraday reactions owing to the surface functional groups of APVPC-2, is insignificant effect in comparison to the double-layer capacitance, which agree well with CV curves[53]. Shown in **Fig. S3c**, the internal cell resistance is 3.087 Ω (82.52 kHz) for APVPC-1 and 3.104 Ω (68.12 kHz) for APVPC-3. The slope of APVPC-2 parallelled to Z'' axis is higher than APVPC-1 and APVPC-3 prepared with different the activation time (1h vs 3h vs 6h, APVPC-1 vs APVPC-2 vs APVPC-3) which reveals few diffusion restriction for electrolyte ions to access to the electrode surface [54]. On account of the slope of the straight line in Nyquist plots, that the order of WAPVPC-2 >WAPVPC-1 >WAPVPC-3 could be deduced. Additionally, the internal cell resistance is 6.289 Ω (68.12 kHz) for APVPC-4 and 5.004 Ω (56.25 kHz) for APVPC-5 as well as 3.349Ω (56.25 kHz) for APVPC-6 (**Fig. S3d**). The slope of APVPC-2 is also the higher than APVPC-4, APVPC-5 and APVPC-6 synthesized with different concentration of H_3PO_4 (1M vs 5M vs 10M vs 16 M H_3PO_4, APVPC-4 vs APVPC-5 vs APVPC-6 vs APVPC-2), which demonstrates the order of WAPVPC-2 > WAPVPC-4 > WAPVPC-6 > WAPVPC-5. On account of electrochemical impedance spectroscopy measurements, it could be deduced that the electrode materials APVPC-2 have low ionic resistance inside the porous structure that promote the fast diffusion of electrolyte ions into the porous network. In addition, the electrode material APVPC-2 reveals good conductivity and low charge transfer resistance that facilitate fast charge transfer between the electrolytes and electrode materials. The results further demonstrate that the APVPC-2 is a promising electrode material for supercapacitor applications.

The capacitive performance of the porous materials are further tested with galvanostatic charge-discharge (GCD) measurements at various current densities in 3M KOH with the voltage windows the same as that of the CV analysis. The GCD curves are almost symmetrical with slight distortion, confirming a good capacitive behavior of electrical double layer capacitance (EDLC) and little pseudo-capacitance, which coincide with the results of CV. As calculated from the GCD curves, APVPC-2 indicates the specific capacitance of a specific capacitance of 966.4 F g^{-1} at 1 A g^{-1} (474.38 F g^{-1} at 1A g^{-1} for PVPC), and further still displays a specific capacitance of 221.6 F g^{-1} even at 20 A g^{-1}, which reveals the good energy storage-output capacity at high current density and further confirms the effect of the activation agent H_3PO_4. The lowered capacitance at higher current densities is also ascribed to the insufficient electrolyte ions diffusion kinetics across the micropores due to the narrow pore size at higher operating current densities, the reduced accumulation amount of electrolyte ions onto porous electrode interface leads to the decrement in specific capacitance[49]. APVPC-2 electrode exhibits high specific capacitance due to the synergistic effect of the rich active heteroatom-doping and suitable pore size distribution. This result also illustrates that the conductivity of the electrode is good, but the pore structure is in favor of K^+ and OH^- ion diffusion. In the KOH aqueous electrolytes solution, the micropores with pore size less than 0.5 nm are usually deemed too narrow for double-layer formation, nevertheless, pores

larger than 2 nm are too wide. Consequently, the APVPC-2 that possesses concentrated pores size distribution of 0.718 nm is very applicable for the delivery of the electrolytes ions in the sample porous channels, and further achieving high electrosorption efficiency, which also could result in improved specific capacitance[55]. In addition, the surface functionalities and incorporation of N, O, P and S hetero atoms in APVPC-2 which have been investigated by XPS could also contribute to high pseudocapacitance[56]. In this context, the graphitic N in APVPC-2 greatly improves electron transport by decreasing the intrinsic resistance, and the pyridinic and pyrrolic N in porous carbon strongly favors rapid ion transport kinetics inside the pores[54]. P-doped configuration of APVPC-2 could inhibit the formation of electrophilic oxygen species but also greatly stabilizes the electrochemical interface of the grapheme electrode[57]. The S hetero atoms can greatly enhance space utilization by promoting the electrosorption of electrolyte ions[58]. The presence of hetero atoms increases the polarity of the pores and thereby facilitates easy contact between pore and electrolyte. In general, co-doping effect of N, P and S could greatly modify the chemical and surface nature of the porous carbon and improve the ion and electron transfer kinetics of carbon, which could contribute to a superior performance. At the same time, the reaction time and concentration of H_3PO_4 could also put effect on the specific capacitance. Fig. 2d-c compares the capacitance retention of all APVPC samples at a range of current density from 1 to 20 A g^{-1}. As the reaction time increases (**Fig. 2d**), the APVPC-2 delivers higher capacitance than APVPC-1 and APVPC-3, which is attributed to the increased pores formed from the activated carbon atoms and the activator with the optimal reaction time (1h vs 3h vs 6h, 474.38 vs 966.4 vs 276.9 F g^{-1}; APVPC-1 vs APVPC-2 vs APVPC-3). With the increase of concentration of H_3PO_4 (**Fig. 2e**), the specific capacitances are also progressively increased in the same way (1M vs 5M vs 10M vs 16M, 506 vs 53.8 vs 475 vs 966.4 F g^{-1}; APVPC-4 vs APVPC-5 vs APVPC-6 vs APVPC-2). When the concentration of H_3PO_4 is relatively low, the amount of activator is inadequate to fully activate the carbon. But with the increase of concentration of H_3PO_4, more carbon can react with the activator and further generate more pores, which eventually contribute to the increases of the specific surface area and the pore volume. In general, APVPC-2 delivers the smaller charge-transfer resistance and larger ion diffusion than other APVPC samples and other previously reported biomass derived porous carbon with aqueous electrolytes[59], which demonstrate that despite moderate micropore surface area, appropriate PSD, rich active heteroatoms contents and good crystallinity make APVPC-2 have the best capacitive performance.

The long-term cyclic stability is a crucial factor for electrode materials in energy storage application. **Fig. 2f** demonstrates the variation of capacitance retention and GCD curves as a function of cycle number for APVPC-2 at a current density of 10 A g^{-1}. The specific capacitance decreases slowly at the first 1000 cycles and maintains at about 95.6% of the initial specific capacitance with a slight fluctuation even after 10000 cycles. Moreover, the differences in the 1st, and 10000th charge-discharge curves are almost fully overlapped except a faint decay, which evidence the excellent cycling stability and the robust structure of these pomelo valves derived porous carbons.

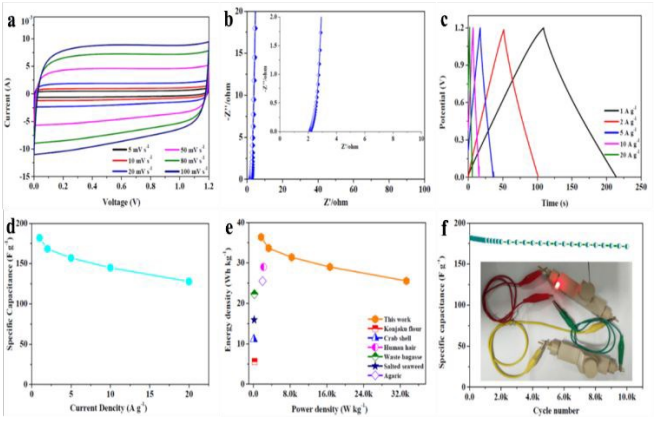

Fig. 3 (a) CV curves of the APVPC//APVPC symmetrical supercapacitor at different scan rates in the voltage window of 0-1.2 V. (b) Nyquist plots of the APVPC//APVPC symmetrical supercapacitor before and after recycling. (c) Galvanostatic charge/discharge curves of the APVPC//APVPC symmetrical supercapacitor at different current densities. (d) Specific capacitances of the as-assembled APVPC symmetrical supercapacitor at different current densities. (e) Ragone plots of the APVPC symmetrical supercapacitor and other previously reported carbon-based symmetric supercapacitors. (f) Cycle performance of the APVPC symmetrical supercapacitor at a current density of 10 A g^{-1} (insert photograph of lighting LED bulbs).

A symmetric two-electrode cell has been assembled to further evaluate the capacitive performance of APVPC-2 in 3 M KOH. The CV curves (**Fig. 3a**) recorded at different current densities from 5 to 100 mV s^{-1}, indicate a quasi-rectangular shape, which demonstrates the formation of good electric double-layer capacitance (EDLC) behavior with fast charge/discharge processes and a good rate electrochemical performance[60]. Meanwhile, there are also no redox peaks/humps due to the pseudocapacitive interaction of ions with functional groups which could be observed. The pseudocapacitance behavior in porous carbon strongly depends on nature of the electrolytes (ex: type and pH) and the effect is almost negligible in neutral and non-aqueous electrolytes[61]. The Nyquist plot for APVPC-2 (**Fig. 3b**) is almost vertical at the low-frequency region, revealing an easy electrolyte diffusion to the surface and good capacitive behavior. Simultaneously, the internal cell resistance (real Z' axis from Nyquist plots) is 2.146 Ω (6.17 kHz) for the supercapacitor. The GC curves (Figure 3c) exhibit perfect symmetric triangle shapes at different current densities, confirming a facile, smooth adsorption/desorption process and further good capacitive characteristics. During the measurement, the change of capacitance from 181.95 to 127.78 A g^{-1} is accompanied with the current density varying from 1 to 20 A g^{-1} (**Fig. 3d**), which reveals a good rate performance with a capacitance retention of 70.22%. The attractive rate capability can be ascribed to the matching between the pore and the electrolyte 3 M KOH. The results are also superior to those from reported carbon-based capacitors[62-63], illustrating that the electrolyte ions could efficiently, rapidly and fully penetrate into the electrochemically active interface of the APVPC-2 carbon material even at a high current density (20 A g^{-1}), which originates from its 3D hierarchically interconnected porous structure. Compared with other energy storage systems, the Ragone plot delivers an energy density of 36.39 W h kg^{-1} at low

power density of 1.67 kW kg^{-1} (**Fig. 3e**). Even at an ultra-high power density of 33.33 kW kg^{-1}, the supercapacitor could still function efficiently with an energy density of 25.56 W h kg^{-1}, which surpass several previously reported systems[64-65]. The superior energy-power output behavior effectively bridges the performance gap between batteries and capacitors. The long cycle life of the supercapacitor is evaluated by constant current charge-discharge cycles at a current density of 10 A g^{-1} as shown in **Fig. 3f**. The energy loss could be calculated to be 5.1% after 10000 cycles, indicating good cycling stability. To further demonstrate the practical application of the as-fabricated SC, a tandem device is assembled by connecting two prototype units in series. Subsequently, the device is used to light up a red light-emitting-diode (LED, the lowest working potential is 2.0 V), as depicted in the inset of **Fig. 3f**. This tentative test suggests the great potential of the APVPC-2 materials for high performance energy storage systems.

4. Conclusions

In conclusion, porous carbon material with interconnected hierarchical pores are derived from a sustainable, low-cost, and environmentally abundant waste pomelo valves biomass precursor by the hydrothermal activation of H_3PO_4 and the simple carbonization. In addition, surface functionalities over the pore wall could be tuned using nitrogen and sulfur as well as phosphorus hetero atoms to achieve excellent electrochemical performance. The electrochemical performance of the porous carbon is superior to that of conventional porous carbon and graphene-based electrodes. The stability and energy-power behavior were among the best reported for any porous carbon. A maximum energy density of 36.39 W h kg^{-1} has been achieved, along with an ultra-high output power of ~25.56 W h kg^{-1}, while retaining an energy density of ~33.33 kW kg^{-1}. Moreover, a long-lasting stability of 10 000 cycles with an energy loss of 5.1% is also demonstrated. The superior performance contributes to a good platform for large-scale production of porous activated carbon networks to achieve high-performance and stable supercapacitors.

Conflicts of interest

There are no conflicts to declare.

Acknowledgements

We gratefully acknowledge to the financial support from Faculty of Materials and Energy and Institute for Clean Energy & Advanced Materials, Southwest University and Chongqing Key Laboratory for Advanced Materials and Technologies of Clean Electrical Power Sources and the Recruitment Program of Southwest University (SWU117023).

References

1 M. Jana, R. Xu, X. B. Cheng, J. S. Yeon, J. M. Park, J. Q. Huang, Q. Zhang, H. S Park, *Energy Environ. Sci*, 2020, **13**, 1049.
2 B. B. Shao, Z. F. Liu, G. M. Zeng, H. Wang, Q. H. Liang, Q. Y. He, M. Cheng, C. Y. Zhou, L. B. Jiang, B. Song, *J. Mater. Chem. A*, 2020, **8**, 7508.
3 Q. Hao, C. W. Liu, G. H. Jia, Y. Wang, H. Arandiyan, W. Wei, B. J. Ni, *Mater. Horiz*, 2020, **7**, 1014.
4 Y. Y. Wang, J. Liu, Y. P. Feng, N. Y. Nie, M. M. Hu, J. Q. Wang, G. X. Pan, J. H. Zhang, Y. Huang, *Chem. Commun*, 2020, 5**6**, 4793.
5 R. J. Young, M. T. Huxley, E. Pardo, N. R. Champness, C. J. Sumby, C. J. Doonan, *Chem. Sci*, 2020, **11**, 4031.
6 J. J. Zhang, H. P. Zhao, J. Li, H. L. Jin, X. C. Yu, Y. Lei, S. Wang, *Adv. Energy Mater*, 2018, **9**, 1803221.
7 L. J. Kong, M. Zhong, W. Shuang, Y. H. Xu, X. H. Bu, *Chem. Soc. Rev*, 2020, **49**, 2378.
8 L. Tong, M. Y. Gao, C. Jiang, K. F. Cai, *J. Mater. Chem. A*, 2019, **7**, 10751.
9 S. S. Qin, Q. Zhang, X. X. Yang, M. M. Liu, Q. J. Sun, Z. L. Wang, *Adv. Energy. Mater*, 2018, **8**, 1800069.
10 M. P. Browne, Z. Sofer, M. Pumera, *Energy Environ. Sci*. 2019, 12, 41.
11 H. J. Zhang, Y. K. Wang, L. B. Kong, *Nanoscale*, 2019, **11**, 7263.
12 J. H. Han, A. Hirata, J. Du, Y. Ito, T. Fujita, S. Kohara, T. Ina, M. W. Chen, *Nano Energy*, 2018, **49**, 354.
13 Z. N. Deng, H. Jiang, C. Z. Li, *Small*, 2018, **14**, 1800148.
14 Y. C. Ding, L. Mo, C. Gao, X. P. Liu, T. Yu, W. Y. Chen, S. H. Chen, Z. Q. Li, L. H. Hu, *ACS Sustainable Chem. Eng*, 2018, **6**, 9822.
15 S. Ramaraj, M. Sakthivel, S. M. Chen, K. C. Ho, *Anal. Chem*, 2019, **91**, 8358.
16 H. L. Jin, J. Li, Y. F. Yuan, J. C. Wang, J. Lu, S. Wang, *Adv. Energy Mater*, 2018, **8**, 1801007.
17 L. F. Chen, Y. Lu, L. Yu, X. W. Lou, *Energy Environ. Sci*, 2017, **10**, 1777.
18 E. Hao, W. Liu, S. Liu, Y. Zhang, H. L. Wang, S. G. Chen, F. L. Cheng, S. P. Zhao, H. Z. Yang, *J. Mater. Chem. A*, 2017, **5**, 2204.
19 J. T. Hu, J. Yang, Y. D. Duan, C. K. Liu, H. T. Tang, L. P. Lin, Y. Lin, H. B. Chen, F. Pan, *Chem. Commun*, 2017, **53**, 857.
20 G. Wang, S. K. Kim, M. C. Wang, T. S. Zhai, S. Munukutla, G. S. Girolami, P. J. Sempsrott, S. Nam, P. V. Braun, J. W. Lyding, *ACS Nano*, 2020, **14**, 632.
21 M. Y. Liu, J. Niu, Z. P. Zhang, M. L. Dou, F. Wang, *Nano Energy*, 2018, **51**, 366.
22 J. J. Xue, T. Wu, Y. Q. Dai, Y. N. Xia, *Chem. Rev*, 2019, **119**, 5298.
23 H. Khani, T. J. Dowell, D. O. Wipf, *ACS Appl. Mater. Interfaces*, 2018, **10**, 21262.
24 S. Y. Lu, M. Jin, Y. Zhang, Y. B. Niu, J. C. Gao, C. M. Li, *Adv. Energy Mater*, 2018, **8**, 1702545.
25 S. Bhattacharya, I. Roy, A. Tice, C. Chapman, R. U, V. Chakrapani, J. L. Plawsky, R. J. Linhardt, *ACS Appl. Mater. Interfaces*, 2020, **12**, 19369.
26 J. Niu, R. Shao, J. J. Liang, M. L. Dou, Z. L. Li, Y. Q. Huang, F. Wang, *Nano Energy*, 2017, **36**, 322.
27 S. H. Chen, L. Qiu, H. M. Cheng, *Chem. Rev*, 2020, **120**, 2811.
28 Y. Gao, J. Zhang, N. Li, X. Han, X. Luo, K. Y. Xie, B. Q. Wei, Z. H. Xia, *J. Mater. Chem. A*, 2020, **8**, 7756.
29 X. K. Huang, X. Y. Sui, W. X. Ji, Y. L. Wang, D. Y. Qu, J. H. Chen, *J. Mater. Chem. A*, 2020, **8**, 7641.
30 L. J. Kong, M. Zhong, W. Shuang, Y. H. Xu, X. H. Bu, *Chem. Soc. Rev*, 2020, **49**, 2378.
31 F. X. Wu, J. Maier, Y. Yu, *Chem. Soc. Rev*, 2020, **49**, 1569.
32 L. Chen, N. J. Luo, S. P. Huang, Y. F. Li, M. D. Wei, *Chem. Commun*, 2020, **56**, 3951.
33 M. Fingerle, H. F. Bettinger, *Chem. Commun*, 2020, **56**, 3847.
34 T. P. Zhou, N. Zhang, C. Z. Wu, Y. Xie, *Energy Environ. Sci*, 2020, **13**, 1132.
35 M. Jana, R. Xu, X. B. Cheng, J. S. Yeon, J. M. Park, J. Q. Huang, Q. Zhang, H. S. Park, *Energy Environ. Sci*, 2020, **13**, 1049.

View Article Online
DOI: 10.1039/D0NA00211A

36 S. A. Hashemi, S. Ramakrishna, A. G. Aberle, *Energy Environ. Sci*, 2020, **13**, 685.
37 T. Deepalakshmi, T. T. Nguyen, N. H. Kim, K. T. Chong, J. H. Lee, *J. Mater. Chem. A*, 2019, **7**, 24462.
38 M. Y. Song, Y. H. Zhou, X. Ren, J. F. Wan, Y. Y. Du, G. Wu, F. W. Ma, *J. Colloid Interface Sci*, 2019, **535**, 276.
39 Q. Chang, M. A. Darabi, Y. Q. Liu, Y. F. He, W. Zhong, K. Mequanin, B. Y. Li, F. Lu, M. M. Q. Xing, *J. Mater. Chem. A*, 2019, **7**, 24626.
40 R. Samal, S. Mondal, A. S. Gangan, B. Chakraborty, C. S. Rout, *Phys. Chem. Chem. Phys*, 2020, **22**, 7903.
41 M. Y. Zhu, J. J. Tang, W. J. Wei, S. J. Li, *Mater. Chem. Front*, 2020, **4**, 1105.
42 T. Y. Liu, P. Diao, Z. Lin, H. L. Wang, *Nano Energy*, 2020, **74**, 104787.
43 B. K. Deka, A. Hazarika, S. Lee, D. Y. Kim, Y. B. Park, H. W. Park, *Nano Energy,* 2020, **73**, 104754.
44 S. Abdolhosseinzadeh, R. Schneider, A. Verma, J. Heier, F. Nüesch, C. F. Zhang, *Adv. Mater,* 2020, **32**, 2000716.
45 S. H. Zheng, X. Y. Shi, P. Das, Z. S. Wu, X. H. Bao, *Adv. Mater*, 2019, **31**, 1970351.
46 Y. S. Zhao, Y. Alsaid, B. W. Yao, Y. C. Zhang, B. Z. Zhang, N. Bhuskute, S. W. Wu, X. M. He, *Adv. Funct. Mater*, 2020, **10**, 1909133.
47 X. R. Li, H. P. Li, X. Q. Fan, X. L. Shi, J. J. Liang, *Adv. Energy Mater*, 2020, **14**, 1903794.
48 R. Z. Hou, M. Miao, Q. Y. Wang, T. Yue, H. F. Liu, H. S. Park, K. Qi, B. Y. Xia, *Adv. Energy Mater*, 2020, **1**, 1901892.
49 M. Y. Wang, S. L. Xie, C. Q. Tang, X. Fang, M. Liao, L. Wang, Y. Zhao, Y. Z. Wen, L. Ye, B. J. Wang, H. S. Peng, *Small*, 2019, **52**, 1905903.
50 H. H. Lu, C. Yang, J. Chen, J. Li, H. l. Jin, J. C. Wang, S. Wang, *Small*, 2020, **17**, 1906584.
51 R. Y. Bi, Nan Xu, H. Ren, N. L. Yang, Y. G. Sun, A. Cao, R. B. Yu, D. Wang, *Angew. Chem. Int. Ed*, 2020, **12**, 4865.
52 J. J. Liu, Y. Zhou, Z. Xie, Y. Li, Y. P. Liu, J. Sun, Y. H. Ma, O. Terasaki, L. Chen, *Angew. Chem. Int. Ed*, 2020, **3**, 962.
53 S. Thurakkal, X. Y. Zhang, *Adv. Sci*, 2020, **2**, 1902359.
54 R. Thangavel, A. G. Kannan, R. Ponraj, V. Thangavel, D. W. Kim, Y. S. Lee, *J. Mater. Chem. A*, 2018, **6**, 17751.
55 R. Thangavel, A. G. Kannan, R. Ponraj, X. L. Sun, D. W. Kim, Y. S. Lee, *J. Mater. Chem. A*, 2018, **6**, 9846.
56 G. J. Guan, M. Y. Han, *Adv. Sci*, 2019, **23**, 1901837.
57 Z. H. Bi, L. Huo, Q. Q. Kong, F. Li, J. P. Chen, A. Ahmad, X. X. Wei, L. J. Xie, C. M. Chen, *ACS Appl. Mater. Interfaces*, 2019, **11**, 11421.
58 J. Edberg, R. Brooke, H. Granberg, I. Engquist, M. Berggren, *Adv. Sus. Sys*, 2019, **8**, 1668.
59 J. H. Zhu, J. Roscow, S. Chandrasekaran, L. B. Deng, P. X. Zhang, T. S. He, K. Wang, L. C. Huang, *ChemSusChem*, 2020, **6**, 1275.
60 W. F. Mao, W. Yue, Z. J. Xu, S. Y. Chang, Q. Q. Hu, F. Pei, X. D. Huang, J. B. Zhang, D. J. Li, G. Liu, G. Ai, *ACS Nano*, 2020, **14**, 4741.
61 C. F. Xue, L. Feng, Y. N. Hao, F. J. Yang, Q. Zhang, X. L. Ma, X. G. Hao, *Green Chem*, 2018, **20**, 4983.
62 Y. X. Liu , Z. C. Xiao , Y. C. Liu, L. Z. Fan, *J. Mater. Chem. A*, 2018, **6**, 160.
63 Y. Zhang, S. S. Liu, X. Y. Zheng, X. Wang, Y. Xu, H. Q. Tang, F. Y. Kang, Q. H. Yang, J. Y. Luo, *Adv. Funct. Mater*, 2017, **27**, 1604687.
64 M. Zohair, K. Moyer, J. E. Rathert, C. Z. Meng, J. Waugh, C. L. Pint, *ACS Nano*, 2020, **14**, 2308.
65 B. J. Zhu, B. Liu, C. Qu, H. Zhang, W. H. Guo, Z. B. Liang, F. Chen, R. Q. Zou, *J. Mater. Chem. A*, 2018, **6**, 1523.

View Article Online
DOI: 10.1039/D0NA00211A